

# Representing statistics of dispersions via moment methods and recurrent neural networks with application to cavitating bubbles

S. H. Bryngelson,<sup>1</sup> A. Charalampopoulos,<sup>2</sup> T. P. Sapsis,<sup>2</sup> R. O. Fox,<sup>3</sup>  
T. Colonius<sup>4</sup>

(<sup>1</sup>Georgia Institute of Technology, <sup>2</sup>Massachusetts Institute of Technology,  
<sup>3</sup>Iowa State University, <sup>4</sup>California Institute of Technology, USA)

## ABSTRACT

The dynamics of cavitation bubbles are important in many applications, but the wide range of spatio-temporal scales and a large number of bubbles often preclude direct simulations. We develop a statistical Euler–Euler description of sub-grid bubbles that includes, for the first time, the independent variables of the oscillatory cavitation dynamics. The approach stitches together several state-of-the-art computational tools: a generalized population balance representing the statics of the cavitating bubbles, conditional quadrature moment methods (QBMMs) computes them, ensemble phase-averaging couples them to the fluid flow, and high-order-accurate interface capturing stably evolves the flow in time. The one-way-coupled evolution of the forced bubbles is used to evaluate the accuracy of the QBMM statistics against truth data generated through a Monte Carlo approach. CHyQMOM provides the most computationally efficient closure for this purpose, and we implement it in the open-source MFC multiphase flow solver.

An acoustically excited bubble screen problem is used to determine the importance and relevance of representing the bubble statistics in this way. Broadening the distribution of bubble radii and radial velocities significantly impacts the dynamics. Broader distributions in radii increase pressure fluctuations, as the averaged bubble oscillations occur at a shorter time scale than the transmitted pressure wave. Broadening the bubble radial velocity distribution results in the opposite effect, smoothing the pressure oscillations observed in the screen region.

Our results also show that significant model-form errors can accumulate under strong and long-time pressure forcings. To address this issue, we present a long short-term memory recurrent neural network (LSTM RNN) model that adjusts the quadrature rule to improve its accuracy. The method is tested on a simple one-way-coupled test

case and shown to decrease these errors by a factor of about ten. The neural network avoids introducing numerical instabilities by incorporating the moment transport equations and the moment realizability into the loss function.

## INTRODUCTION

Flowing dispersions of oscillating bubbles display dynamics at a broad range of spatio-temporal scales. Computational models can alleviate simulation costs by representing the dynamics of the dispersed phase at the sub-grid level instead of resolving them directly. Population balance models are a statistical framework for this (Vanni, 2000). They solve a population balance equation (PBE) by, e.g., the method of moments, which approximates the evolving PBE quantities using a set of statistical moments (McGraw, 1997). This approach has successfully modeled the coalescence, breakup, and motion of the dispersed phase (Fox, 2008). This is useful for simulating the soot that forms from combustion processes (Mueller et al., 2009), aerosol sprays (Sibra et al., 2017), and more.

We implement a conditional moment method called CHyQMOM into a high-order-accurate multiphase flow solver called MFC. The method can interrogate two-way-coupled fluid–bubble interactions. We assess this via an acoustically excited bubble screen problem. At the same time, model-form errors can be meaningfully large for strong pressure forcings (Bryngelson et al., 2020). Some moment methods can accommodate arbitrarily large moment sets to better approximate high-order statistics of the dynamics (McGraw, 1997; Yuan and Fox, 2011). However, these methods can become numerically stiff or unstable. For quadrature-based moment methods, this happens when the quadrature nodes become arbitrarily

close to each other and the moment set becomes unrealizable (Vikas et al., 2011). We explore long short-term memory (LSTM) recurrent neural networks (RNNs) as an approach to overcome this limitation. Cavitating bubble dispersions are used as a case study since non-Gaussian features are essential for strong driving pressures (Bryngelson et al., 2020).

A previous study used an LSTM RNN to extrapolate high-order moments from Gaussian ones for this problem (Bryngelson et al., 2020). We expand on this study by considering quadrature moment methods instead of strictly Gaussian ones. Besides increased accuracy for the same computational cost, this change allows for data-driven corrections to the quadrature rule directly and incorporates the high-order moments into the neural network loss function.

## MODEL FORMULATION

### Compressible flow equations

A dilute suspension of dynamically evolving bubbles flow in a compressible liquid is considered. For simplicity, we assume no slip between the bubbles and the surrounding liquid and that the gas density is much smaller than the liquid density. Under these assumptions, the mixture-averaged form of the compressible flow equations are

$$\begin{aligned} \frac{\partial \rho}{\partial t} + \nabla \cdot (\rho \mathbf{u}) &= 0, \\ \frac{\partial \rho \mathbf{u}}{\partial t} + \nabla \cdot (\rho \mathbf{u} \mathbf{u} + p \mathbf{I}) &= 0, \\ \frac{\partial E}{\partial t} + \nabla \cdot (E + p) \mathbf{u} &= 0, \end{aligned} \quad (1)$$

where  $\rho$ ,  $\mathbf{u}$ ,  $p$ , and  $E$  are the density, velocity vector, pressure, and total energy. Terms associated with the bubbles modify these quantities and transport them in space according to ensemble phase-averaging, discussed next.

### Ensemble phase-averaging

The ensemble-averaged equations follow from a standard analysis (Zhang and Prosperetti, 1994; Ando et al., 2011; Bryngelson et al., 2019). The disperse phase has a void fraction  $\alpha$  and is assumed to be a dilute ( $\alpha \ll 1$ ) population of spherical bubbles. The bubbles are represented statistically via random variables  $R$ ,  $\dot{R}$ , and  $R_o$  corresponding to the instantaneous bubble radius, time

derivative, and equilibrium bubble radius, presented in the next section. The mixture-averaged pressure field is computed as

$$p(\mathbf{x}, t) = (1 - \alpha)p_\ell + \alpha \left( \frac{\overline{R^3 p_{bw}}}{\overline{R^3}} - \rho \frac{\overline{R^3 \dot{R}^2}}{\overline{R^3}} \right), \quad (2)$$

where  $p_{bw}$  are the associated bubble wall pressure and  $p_\ell(\mathbf{x}, t)$  is the liquid pressure according to the stiffened-gas equation of state (Menikoff and Plohr, 1989):

$$\Gamma_\ell p_\ell + \Pi_{\infty, \ell} = \frac{1}{1 - \alpha} \left( E - \frac{1}{2} \rho \mathbf{u}^2 \right). \quad (3)$$

The coefficients of (3) represent water, with specific heat ratio  $\gamma_\ell = 1 + 1/\Gamma_\ell = 7.15$  and stiffness  $\Pi_{\infty, \ell} = 356$  MPa (Maeda and Colonius, 2018).

The bubble number density per unit volume  $n(\mathbf{x}, t)$  is conserved in the absence of coalescence or breakup:

$$\frac{\partial n}{\partial t} + \nabla \cdot (n \mathbf{u}) = 0. \quad (4)$$

For the spherical bubbles considered here,  $n$  is related to the void fraction  $\alpha$  via

$$\alpha(\mathbf{x}, t) = \frac{4}{3} \pi \overline{R^3} n(\mathbf{x}, t), \quad (5)$$

and thus the void fraction  $\alpha(\mathbf{x}, t)$  transports as

$$\frac{\partial \alpha}{\partial t} + \mathbf{u} \cdot \nabla \alpha = 3\alpha \frac{\overline{R^2 \dot{R}}}{\overline{R^3}}, \quad (6)$$

where the right-hand-side represents the change in void fraction due to bubble growth and collapse.

The over-barred terms appearing in (2), (5), and (6),

$$\overline{R^3 \dot{R}^2}, \quad \overline{R^3}, \quad \overline{R^2 \dot{R}}, \quad \text{and} \quad \overline{R^3 p_{bw}}. \quad (7)$$

denote average quantities of the bubble dispersion. In particular, they are raw moments  $\mu_{lmn}$  with respect to a bubble number density function  $f(R, \dot{R}, R_o)$ ,

$$\begin{aligned} \mu_{lmn} &= \overline{R^l \dot{R}^m R_o^n} = \\ &= \int_{\Omega} R^l \dot{R}^m R_o^n f(R, \dot{R}, R_o) dR d\dot{R} dR_o, \end{aligned} \quad (8)$$

which are computed via the quadrature moment methods of the previous section.

### Bubble dynamics model

We use a simple Rayleigh–Plesset-like bubble dynamics model. Cognizant that many more complex and comprehensive models exist, the RPE model is sufficient to interrogate our method while maintaining sufficient generality

in the implementation. This model assumes spherical bubbles filled with noncondensable gas and incompressible surrounding liquid. Under these assumptions, the bubble radius is governed by a Rayleigh–Plesset-like equation

$$R\ddot{R} + \frac{3}{2}\dot{R}^2 + \frac{4}{\text{Re}}\frac{\dot{R}}{R} = \left(\frac{R_o}{R}\right)^{3\gamma} - \frac{1}{C_p} - \frac{2}{\text{We}R_o} \left[ \frac{R_o}{R} - \left(\frac{R_o}{R}\right)^{3\gamma} \right], \quad (9)$$

which is dimensionless via the reference bubble size  $R_o^*$ , liquid pressure  $p_0$ , and density  $\rho_0$ . The polytropic index is  $\gamma = 1.4$  and  $C_p \equiv p_0/p_\ell$  is the forcing pressure ratio. The Reynolds and Weber numbers are introduced to quantify viscous and surface tension effects as

$$\text{Re} \equiv \sqrt{\frac{p_0}{\rho_0}} \frac{R_o^*}{\nu_0} \quad \text{and} \quad \text{We} \equiv \frac{p_0 R_o^*}{S}, \quad (10)$$

$\nu_0$  is the kinematic viscosity and  $S$  is the surface tension coefficient. Thus,  $p_{bw} = (R_o/R)^{3\gamma}$  and the last moment of (7) is  $\bar{R}^3(R_o/R)^{3\gamma}$ .

## POPULATION BALANCE FORMULATION AND INVERSION

The population balance equation (PBE)

$$\frac{\partial f}{\partial t} + \frac{\partial}{\partial R}(f\dot{R}) + \frac{\partial}{\partial \dot{R}}(f\ddot{R}) = 0 \quad (11)$$

governs the PDF  $f(R, \dot{R}|R_o)$ . One can add coalescence and breakup terms on the right-hand side if needed. Figure 1 summarizes the PBE-based approach.

A set of raw moments  $\vec{\mu}$  represents the number density function  $f$  (Fox, 2003). These moments  $\vec{\mu}$  transport on the grid and evolve according to

$$\frac{\partial n\vec{\mu}}{\partial t} + \nabla \cdot (n\vec{\mu}\mathbf{u}) = n\dot{\vec{\mu}} = n\vec{g} \quad (12)$$

where

$$g_{lmn} = l\mu_{l-1,m+1,n} + m \iiint_{\Omega} \ddot{R} R^l \dot{R}^{m-1} R_o^n f(\vec{\mu}) dR d\dot{R} dR_o \quad (13)$$

and  $\Omega = \Omega_R \times \Omega_{\dot{R}} \times \Omega_{R_o} = (0, \infty) \times (-\infty, \infty) \times (0, \infty)$  (Bryngelson et al., 2020). The integrand of (13) is closed via (9), and the integral is computed via quadrature, as discussed next.

The number density function is split as

$$f(R, \dot{R}, R_o) = f(R, \dot{R}|R_o)f(R_o), \quad (14)$$

and the raw moments are

$$\mu_{lmn} \equiv \int_{\Omega_{R_o}} f(R_o) R_o^m \mu_{lm}(R_o) dR_o \quad (15)$$

$$\approx \sum_{i=1}^{N_{R_o}} w_i \hat{R}_{o,i}^n \mu_{lm}(\hat{R}_{o,i}), \quad (16)$$

where  $N_{R_o}$  is the number of  $R_o$ -direction weights  $w_i$  and abscissas  $\hat{R}_{o,i}$ , which are computed via Simpson's rule for the results here. The  $R_o$ -conditioned moments are

$$\mu_{lm}(\hat{R}_{o,i}) \equiv \iint_{\Omega_{R,\dot{R}}} f(R, \dot{R}|\hat{R}_{o,i}) R^l \dot{R}^m dR d\dot{R} \approx \sum_{j=1}^{N_R} \sum_{k=1}^{N_{\dot{R}}} \left[ \hat{w}_{j,k} \hat{R}_j^l \hat{R}_k^m \right]_{\hat{R}_{o,i}}. \quad (17)$$

The moment indices comprising the moment set of (17) are associated with the conditional quadrature moment method used to invert those moments (Yuan and Fox, 2011; Patel et al., 2019). In particular,  $\mu_{lm}(\hat{R}_{o,i})$  is inverted for quadrature points  $\{\hat{R}_j, \hat{R}_k\}(\hat{R}_{o,i})$  and weights  $\hat{w}_{j,k}(\hat{R}_{o,i})$  for each  $i = 1, \dots, N_{R_o}$  (with  $j = 1, \dots, N_R; k = 1, \dots, N_{\dot{R}}$ ). The total moments (16) are approximated by substituting (17) into (16):

$$\mu_{lmn} = \sum_{i=1}^{N_{R_o}} w_i \hat{R}_{o,i}^n \sum_{j=1}^{N_R} \sum_{k=1}^{N_{\dot{R}}} \left[ \hat{w}_{j,k} \hat{R}_j^l \hat{R}_k^m \right]_{\hat{R}_{o,i}}. \quad (18)$$

The CHyQMOM algorithm is described in Fox et al. (2018).

## INTERFACE-CAPTURING METHOD

## NUMERICAL METHOD

Interface-capturing numerics are used to solve for the flow of a polydisperse bubble cloud. The method of the previous section is implemented in MFC, an open-source flow solver (Bryngelson et al., 2021). The governing equations combine as

$$\frac{\partial \vec{q}_c}{\partial t} + \nabla \cdot \vec{F} = \vec{r} \quad (19)$$

where  $\vec{q}_c$  are the conservative variables,  $\vec{F}$  are the advective fluxes, and  $\vec{r}$  are diffusive source terms. The flow is initialized via an independently distributed  $f(R, \dot{R}, R_o)$  with log-normal, normal, and log-normal shapes in the  $R$ ,  $\dot{R}$ , and  $R_o$  directions with expected values  $\mathbb{E}[R] = \mathbb{E}[R_o] = 1$  and  $\mathbb{E}[\dot{R}] = 0$  and shape parameters  $\sigma$ . The moment set  $\vec{\mu}$  is then computed via integration

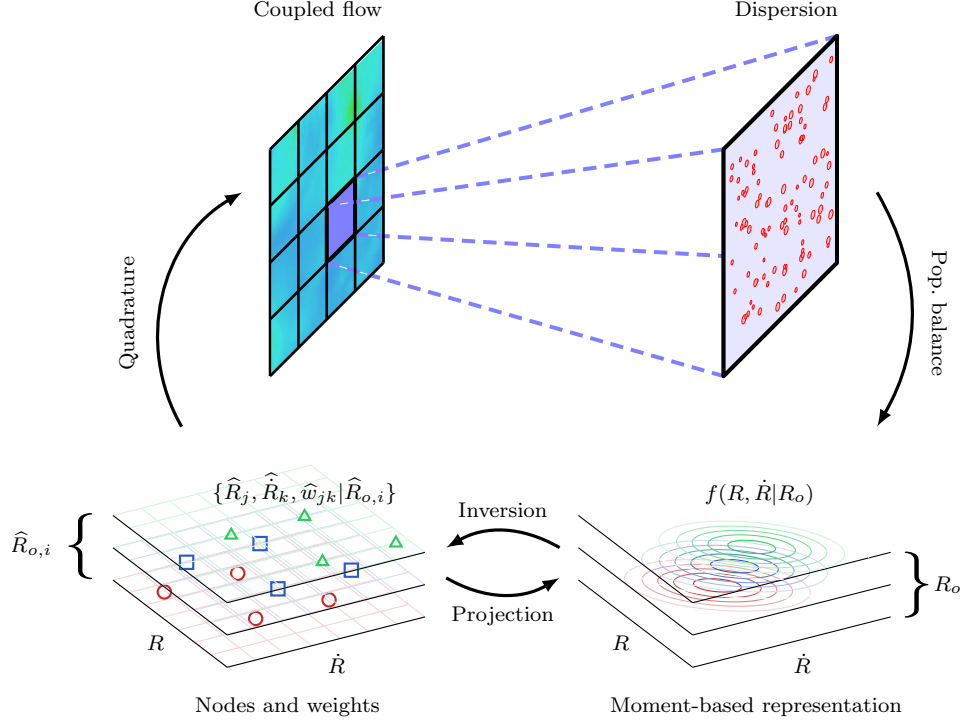


**Figure 1:** Schematic illustration of a quadrature moment method. Adapted from our previous work (Bryngelson et al., 2020).

of the NDF. A fifth-order-accurate WENO (Jiang and Shu, 1996) scheme reconstructs the primitive variables  $\vec{q}_p$  and the HLLC approximate Riemann solver (Toro et al., 1994) computes the fluxes. High-order WENO reconstructions do not guarantee that the reconstructed moments are realizable, though the moment sets remained invertible in the subsequent simulations. The conservative variables are integrated in time using third-order-accurate SSP–RK3 time integration (Gottlieb et al., 2001).

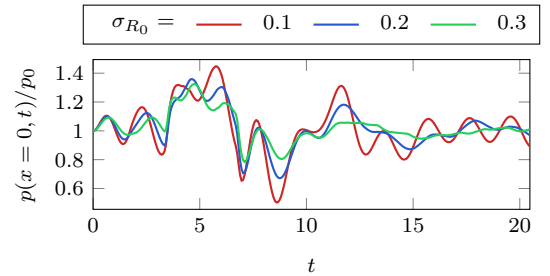
## APPLICATION TO POLYDISPERSE BUBBLE SCREENS

### Problem setup

We assess our approach by considering statistics of bubble dynamics in an acoustically excited dilute bubble screen. The bubble screen parameterization matches that of Bryngelson et al. (2019) and Bryngelson et al. (2021), with initial void fraction  $\alpha_o = 10^{-4}$ , median bubble equilibrium size  $R_o^* = 10 \mu\text{m}$  and log-normal variance  $\sigma_{R_o}$ . A one-way sound wave with pressure  $p_\infty(t)$  is generated via source terms in the governing equations

according to Bryngelson et al. (2019). Its form is a single period of a sinusoid with peak amplitude  $0.3p_0$  and frequency 300 kHz.

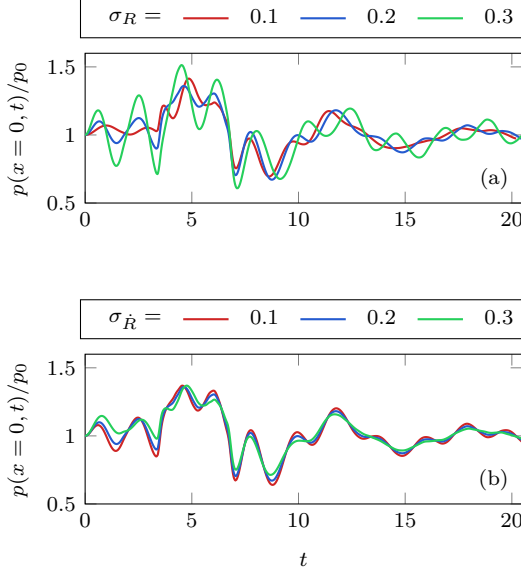
### Bubble screen behavior



**Figure 2:** Bubble-screen-centered pressure for varying  $R_o$  log-normal distributions with shape parameter  $\sigma_{R_o}$  and fixed  $\sigma_R = \sigma_{\dot{R}} = 0.2$ .

We start by considering a screen with fixed dynamic coordinate distributions  $\sigma_R = \sigma_{\dot{R}}$ , but varying distributions of equilibrium sizes  $\sigma_{R_o}$ . Polydispersity in  $R_o$  is integrated via Simpson’s rule 61 quadrature points for all

cases. Figure 2 shows the bubble screen pressure for these cases as they evolve in time. For larger  $\sigma_{R_o}$  (or broader distributions or bubble equilibrium sizes), the pressure is less oscillatory in time. A similar observation was made by Bryngelson et al. (2019) for cases with no  $R$  or  $\dot{R}$  distributions. In the case of figure 2, we instead observe high-frequency oscillations in addition to the long-wavelength behaviors associated with the impinging pressure wave  $p_\infty$ . The origin of these oscillations is discussed next.



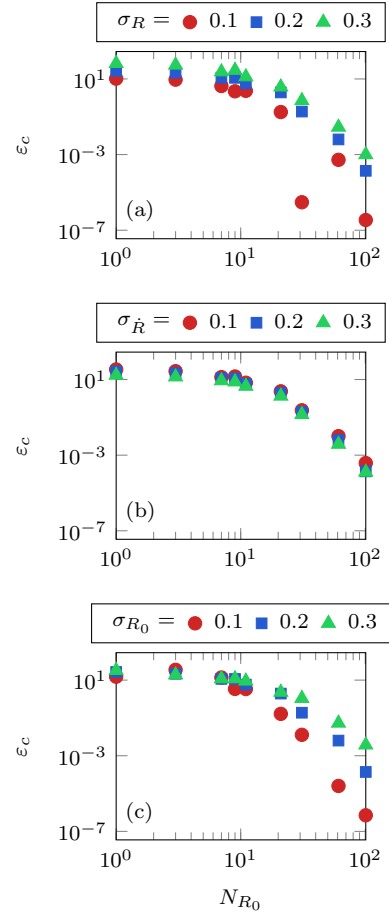
**Figure 3:** Bubble-screen-centered pressure before, during, and after excitement due to an acoustic wave. The bubbles are polydisperse with log-normal  $R_o$  distribution ( $\sigma_{R_o} = 0.2$ ) and  $Re = 10^3$ . Variations in (a)  $\sigma_R$  and (b)  $\sigma_{\dot{R}}$  are shown about a  $\sigma_R = \sigma_{\dot{R}} = 0.2$  representative state.

Figure 3 shows the dynamics associated with a bubble screen in varying degrees of statistical disequilibrium, represented via different  $\sigma_R$  and  $\sigma_{\dot{R}}$ . Figure 3 (a) fixes  $\sigma_{\dot{R}}$  and varies  $\sigma_R$ . We observe the shorter-wavelength oscillatory behavior, observed in figure 2, becoming more prominent for larger  $\sigma_R$ . These wavelengths are commensurate with the mean bubble natural frequencies, which superimpose the longer wavelength acoustics associated with the impinging  $p_\infty$  wave. Figure 3 (b) shows a smoother pressure profile for larger  $\sigma_{\dot{R}}$ . Phase-cancellation between the larger waves associated with broader  $\sigma_{\dot{R}}$  distributions and those of the  $\sigma_R$  distributions may account for this behavior. Notably, these behaviors are qualitatively similar to those associated with varying  $R_o$  distribution widths. Thus, parameterizing an  $R_o$  distribution based on single-probe pressure measurements is insufficient.

## Closure errors

We quantify the moment closure error,  $\varepsilon_c$ , via the relative mismatch in bubble screen pressure  $p(t, x = 0)$  due to truncated  $R_o$  integration as

$$\varepsilon_c \equiv \frac{1}{N_t} \sqrt{\sum_{i=1}^{N_t} \left[ \frac{p^{\text{QBMM}}(t_i, 0) - p^{\text{Ex.}}(t_i, 0)}{p^{\text{Ex.}}(t_i, 0)} \right]^2}. \quad (20)$$



**Figure 4:** Relative closure error  $\varepsilon_c$  (defined in (20)) for increasing number of  $R_o$ -direction quadrature points  $N_{R_o}$ . Variations in (a)  $\sigma_R$ , (b)  $\sigma_{\dot{R}}$ , and (c)  $\sigma_{R_o}$  are shown. Unless labeled otherwise, cases have the baseline  $\sigma_R = \sigma_{\dot{R}} = \sigma_{R_o} = 0.2$ .

Figure 4 shows the  $N_{R_o}$  closure errors associated with variations in all three PDF directions (panels a–c). For varying  $\sigma_R$  (a) and  $\sigma_{R_o}$  (c) we see that increasing variance  $\sigma$  results in larger closure errors, seemingly associated with the larger pressure oscillations. For figure 4 (b), the reverse trend is observed, and larger  $\sigma_{\dot{R}}$  corresponds

to smaller closure errors. This effect matches that of the  $R$ - and  $R_o$ -direction effects, where larger  $\sigma_{\dot{R}}$  results in smoother pressure histories.

## HYBRID QUADRATURE MOMENT METHOD FORMULATION

One cannot reduce the closure errors of figure 4 by adding additional quadrature points, as this makes the simulations either stiff or unstable. Instead, we implement a machine-learning-based hybrid approach following (Charalampopoulos et al., 2021). We improve the CHyQMOM moment inversion by adjusting the location and weights of the quadrature rule. The unaugmented CHyQMOM quadrature rule is denoted via  $\{\mathbf{w}^{(\text{QBMM})}, \boldsymbol{\xi}^{(\text{QBMM})}\}$ . For these corrections, an LSTM RNN is employed. The LSTM is used to incorporate memory effects into the reduced-order model.

The corrections  $\{\mathbf{w}', \boldsymbol{\xi}'\}$  serve as input predictions for the first- and second-order moments as well as the pressure  $\{\mu_{1,0}, \mu_{0,1}, \mu_{2,0}, \mu_{1,1}, \mu_{0,2}, C_p\}$ . They are modeled as

$$\{\mathbf{w}'(t), \boldsymbol{\xi}'(t)\} = \mathbb{G}[\Theta; \boldsymbol{\mu}(\chi(t)), C_p(\chi(t)), \text{Re}], \quad (21)$$

where the vector  $\Theta$  denotes hyperparameters and optimized parameters of the neural network as obtained during training. The chosen hyperparameters are in table 1.

Hyperparameter	Value
Epochs	500
Learning rate	$10^{-5}$
Batch size	32
Activation function	tanh
Recurrent activation function	hard sigmoid
Dropout coefficient	0.10
Recurrent dropout coefficient	0.10
LSTM is stateful	True
Kernel initializer	Zeros
Recurrent initializer	Zeros
Bias initializer	Zeros
Hidden units	28

**Table 1:** Hyperparameters used to train the neural networks.

The history of the reduced-order model states is then

$$\chi(t) = \{t, t - \tau_1, \dots, t - \tau_N\}. \quad (22)$$

and hybrid quadrature rule follows as

$$\mathbf{w} = \mathbf{w}^{(\text{QBMM})} + \mathbf{w}' \quad (23)$$

$$\text{and} \quad (24)$$

$$\boldsymbol{\xi} = \boldsymbol{\xi}^{(\text{QBMM})} + \boldsymbol{\xi}'. \quad (25)$$

The neural network loss function incorporates the high-order moments associated with the ensemble-averaged closure model, the low-order moments  $\boldsymbol{\mu}$ , and the right-hand-side of (13) as

$$\begin{aligned} \mathcal{L} = & \sum_{0 \leq i, j \leq 2} \alpha_{i,j} \left( \frac{\partial \mu_{i,j}^{(\text{ML})}}{\partial t} - \frac{\partial \mu_{i,j}^{(\text{MC})}}{\partial t} \right)^2 + \\ & \sum_{(i,j) \in \mathcal{I}} \beta_{i,j} \left( \sum_k w_k \xi_{1,k}^i \xi_{2,k}^j - \mu_{i,j}^{(\text{MC})} \right)^2 \\ & + \lambda \sum_k \text{Relu}(-w_k), \end{aligned} \quad (26)$$

where,

$$\mathcal{I} = \{(0,0), (1,0), (0,1), (2,0), (1,1), (0,2), (3,0), (2,1), (3,2), (3-3\gamma,0)\}, \quad (27)$$

and

$$\alpha_{i,j} = \left\| \frac{\partial \mu_{i,j}^{(\text{MC})}}{\partial t} \right\|_{\infty}^{-1}, \quad \beta_{i,j} = \left\| \mu_{i,j}^{(\text{MC})} \right\|_{\infty}^{-1}. \quad (28)$$

The first term in (26)  $L_2$  minimizes the right-hand-sides of the transport equations. The second term in (26) minimizes prediction error for the moments and penalizes the network when the weights do not sum to unity. The last term in (26) penalizes negative weights. Once trained,

$$\boldsymbol{\mu} \xrightarrow{(\text{ML})} \{\mathbf{w}, \boldsymbol{\xi}\}$$

is a new quadrature rule that evaluates the right-hand side of the moment transport equations.

## HYBRID CHyQMOM TRAINING

### Pressure signals

The neural network is trained on a broad range of physically viable pressure profiles  $C_p(t)$  as

$$C_p(t) = 1 + \sum_{i=1}^N \alpha_i \sin[2\pi f_i t + \phi_i], \quad (29)$$

where  $t$  corresponds to nondimensional time,  $f_i$  are the dimensionless frequencies, and  $\alpha_i$  and  $\phi_i$  are the corresponding amplitude and phase.  $C_p = 1$  is the equilibrium pressure of the bubbles (for which  $R = 1$  and



$\dot{R} = 0$ ). Most flows do not contain pressure frequencies higher than the natural oscillation frequency of the bubbles (Brennen, 2014). We operate under this constraint, though higher frequencies could be included if desired. On the other hand, very low frequencies are uninteresting because they cause the bubbles to evolve quasi-statically. Hence, without loss of generality, the dimensionless frequencies of  $C_p$  are in the interval  $f_i \in [1/10, 1/5]$ . The phases of the waveforms are independently sampled from a uniform distribution.

### LSTM RNN training procedure

We simulate 1000 samples of individual bubbles for each realization of  $C_p$ . Each case is evolved until  $t = 50$  natural periods of bubble oscillations. The individual bubble dynamics are then averaged to obtain the Monte Carlo reference statistics for each realization. 200 samples of  $C_p$  from (29) are used. From these, 50 are randomly selected for training, with the remaining 150 cases used during testing. The Adam method (Kingma and Ba, 2014) trained each neural network for 500 epochs, minimizing the loss function (26).

Figure 5 shows  $f$  and the quadrature points for one pressure profile at different time instances. The same figure displays the CHyQMOM nodes as estimated by the standard 4-node CHyQMOM scheme and the 4-node hybrid scheme.

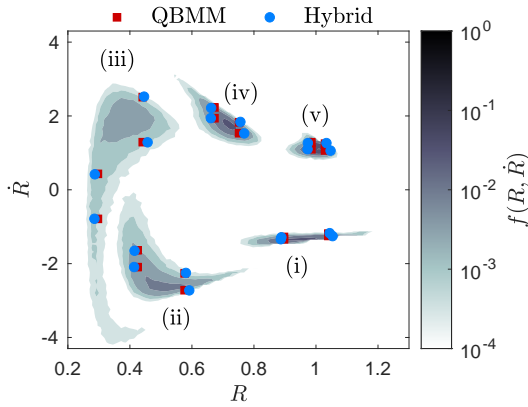


**Figure 5:** Temporal snapshots of  $f$  computed via Monte Carlo and the positions of the quadrature nodes for 4-node CHyQMOM scheme (QBMM) and the hybrid CHyQMOM scheme (Hybrid). The labels (i)–(v) correspond to different times  $t$ .

## HYBRID CHyQMOM RESULTS

### Low-order moment evolution and error quantification

The model-form relative error  $\varepsilon$  is computed via a discrete  $L_2$  error, for which Monte Carlo data serves as the surrogate truth. The  $t_i$  are  $N_t = 5000$  uniformly spaced times in the interval  $t \in [0, 50]$ . Results regarding the low-order moments are presented in figure 6.

Figure 6 shows  $\varepsilon_{l,m}$  for the first- and second-order moments  $\mu$  for the 4-node schemes. All results correspond to 4 randomly selected testing samples (a)–(d) as labeled. We observe a smaller  $\varepsilon$  for the hybrid scheme than standard CHyQMOM for all 4 cases considered. The largest errors for both approaches appear for moment  $\mu_{0,2}$ , which exhibits large and intermittent fluctuations when the bubbles collapse. The observed increase in accuracy varies significantly from case-to-case and moment-to-moment, from 10 times smaller errors to only 20% improvements.

### High-order moment extrapolation

The following quantity of interest is the  $L^2$ -error in predicting the ensemble-averaging-required higher-order moments. Figure 7 presents these results for the same four pressure samples of figure 6. For all moments, the hybrid CHyQMOM significantly improves the predictions of the moments. This improvement is associated with the more accurate evolution of the low-order moments  $\mu$  and these targeted moments in the neural network training procedure.

## DISCUSSION AND CONCLUSIONS

We presented an Euler–Euler simulation algorithm for the statistics of phase-averaged bubbly flows. We showed a conditional quadrature moment method to be efficient for this task, compared to other techniques and other methodologies. The method was integrated into MFC and displayed rich dynamics that are otherwise unrepresented by other simulations of bubbly flows. Even lacking experimental validation, a future aim, this observation is sufficient to warrant further interrogation of the practical, realized statistics of bubbly cavitating flows.

Though our simulations were crafted such that model-form errors were small, larger pressure waves or different

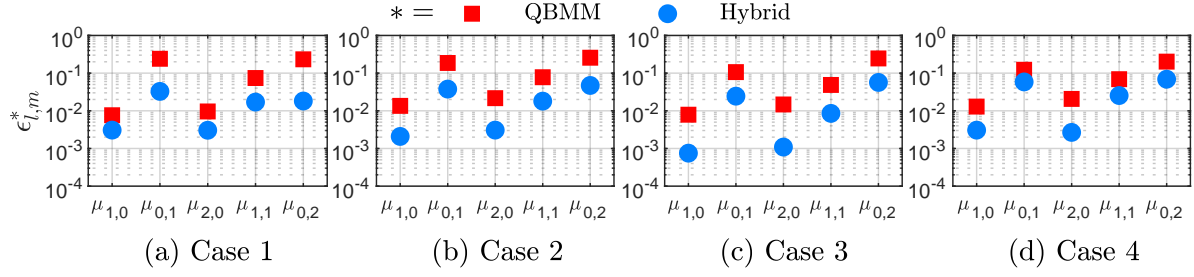


**Figure 6:** Low-order moment errors for different randomly selected test cases (a–d) and the hybrid and standard CHyQMOM as labeled.

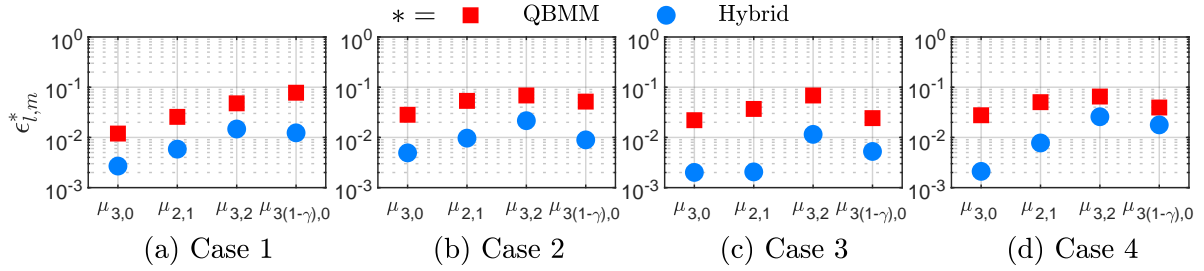


**Figure 7:** High-order moment errors for different randomly selected test cases (a–d) and the hybrid and standard CHyQMOM as labeled.

initial bubble cloud statistics introduce more significant errors. These errors cannot be addressed in the usual way, adding more quadrature points, as we observed numerical instability when attempting to do so. This resulted from quadrature points becoming arbitrarily close together or far apart. Instead, we trained an LSTM RNN with a loss function crafted to adjust the quadrature for more stable, realizable results. This resulted in a significant reduction in model form errors, particularly for the higher-order moments associated with the phase averaging.

## ACKNOWLEDGMENTS

The US Office of Naval Research supported this work under grant numbers N0014-17-1-2676 and N0014-18-1-2625. Computations were performed via the Extreme Science and Engineering Discovery Environment (XSEDE) under allocations TG-CTS120005 (PI Colonius) and TG-PHY210084 (PI Bryngelson), supported by National Science Foundation grant number ACI-1548562.

## REFERENCES

- M. Vanni, Approximate population balance equations for aggregation breakage processes, *J. Colloid Interface Sci.* 221 (2000) 143–160.
- R. McGraw, Description of aerosol dynamics by the quadrature method of moments, *Aerosol Sci. Technol.* 27 (1997) 255–265.
- R. O. Fox, A quadrature-based third-order moment method for dilute gas–particle flows, *J. Comp. Phys.* 227 (2008) 6313–6350.
- M. E. Mueller, G. Blanquart, H. Pitsch, A joint volume-surface model of soot aggregation with the method of moments, *Proc. Combust. Inst.* 32 I (2009) 785–792.
- A. Sibra, J. Dupays, A. Murrone, F. Laurent, M. Massot, Simulation of reactive polydisperse sprays strongly coupled to unsteady flows in solid rocket motors: Efficient strategy using Eulerian multi-fluid methods, *J. Comp. Phys.* 339 (2017) 210–246.
- S. H. Bryngelson, A. Charalampopoulos, T. P. Sapsis, T. Colonius, A Gaussian moment method and its augmentation via LSTM recurrent neural networks for the statistics of cavitating bubble populations, *Int. J. Mult. Flow* 127 (2020) 103262.
- C. Yuan, R. O. Fox, Conditional quadrature method of moments for kinetic equations, *J. Comp. Phys.* 230 (2011) 8216–8246.
- V. Vikas, Z. J. Wang, A. Passalacqua, R. O. Fox, Realizable high-order finite volume schemes for quadrature-



- based moment methods, J. Comp. Phys. 230 (2011) 5328–5352.
- D. Z. Zhang, A. Prosperetti, Ensemble phase-averaged equations for bubbly flows, Phys. Fluids 6 (1994).
- K. Ando, T. Colonius, C. E. Brennen, Numerical simulation of shock propagation in a polydisperse bubbly liquid, Int. J. Mult. Flow 37 (2011) 596–608.
- S. H. Bryngelson, K. Schmidmayer, T. Colonius, A quantitative comparison of phase-averaged models for bubbly, cavitating flows, Int. J. Mult. Flow 115 (2019) 137–143.
- R. Menikoff, B. J. Plohr, The Riemann problem for fluid-flow of real materials, Rev. Mod. Phys. 61 (1989) 75–130.
- K. Maeda, T. Colonius, Eulerian–Lagrangian method for simulation of cloud cavitation, J. Comp. Phys. 371 (2018) 994–1017.
- S. H. Bryngelson, T. Colonius, R. O. Fox, QBMM-lib: A library of quadrature-based moment methods, SoftwareX 12 (2020) 100615.
- R. O. Fox, Computational models for turbulent reacting flows, Cambridge University Press, 2003.
- R. G. Patel, O. Desjardins, R. O. Fox, Three-dimensional conditional hyperbolic quadrature method of moments, J. Comp. Phys. X 1 (2019) 100006.
- R. O. Fox, F. Laurent, A. Vié, Conditional hyperbolic quadrature method of moments for kinetic equations, J. Comp. Phys. 365 (2018) 269–293.
- S. H. Bryngelson, K. Schmidmayer, V. Coralic, J. C. Meng, K. Maeda, T. Colonius, MFC: An open-source high-order multi-component, multi-phase, and multi-scale compressible flow solver, Comp. Phys. Comm. (2021) 107396.
- G.-S. Jiang, C.-W. Shu, Efficient implementation of weighted eno schemes, J. Comp. Phys. 126 (1996) 202–228.
- E. Toro, M. Spruce, W. Speares, Restoration of the contact surface in the HLL-Riemann solver, Shock waves 4 (1994) 25–34.
- S. Gottlieb, C. W. Shu, E. Tadmor, Strong stability-preserving high-order time discretization methods, SIAM Rev. (2001).
- S. H. Bryngelson, R. O. Fox, T. Colonius, Conditional moment methods for polydisperse cavitating flows, arXiv:2112.14172 (2021).
- A.-T. Charalampopoulos, S. H. Bryngelson, T. Colonius, T. P. Sapsis, Hybrid quadrature moment method for accurate and stable representation of non-Gaussian processes and their dynamics, arXiv:2110.01374 (2021).
- C. E. Brennen, Cavitation and bubble dynamics, Cambridge University Press, 2014.
- D. P. Kingma, J. Ba, Adam: A method for stochastic optimization, arXiv:1412.6980 (2014).